Electronic Supplementary Material (ESI) for RSC Advances.

Supporting Information

Formation of carbon-coated $ZnFe_2O_4$ nanowires and their highly reversible lithium storage properties

By *Jong Guk Kim,[a,b] Youngmin Kim,[a,b] Yuseong Noh,[a,b] and Won Bae Kim*[a,b]*

[a]School of Materials Science and Engineering, Gwangju Institute of Science and Technology (GIST), 261 Cheomdan-gwagiro, Buk-gu, Gwangju 500-712, South Korea

[b]Research Institute for Solar and Sustainable Energies (RISE), Gwangju Institute of Science and Technology (GIST), 261 Cheomdan-gwagiro, Buk-gu, Gwangju 500-712, South Korea

* Corresponding Author: Tel: +82-62-715-2317. Fax: +82-62-715-2304,

E-mail: wbkim@gist.ac.kr

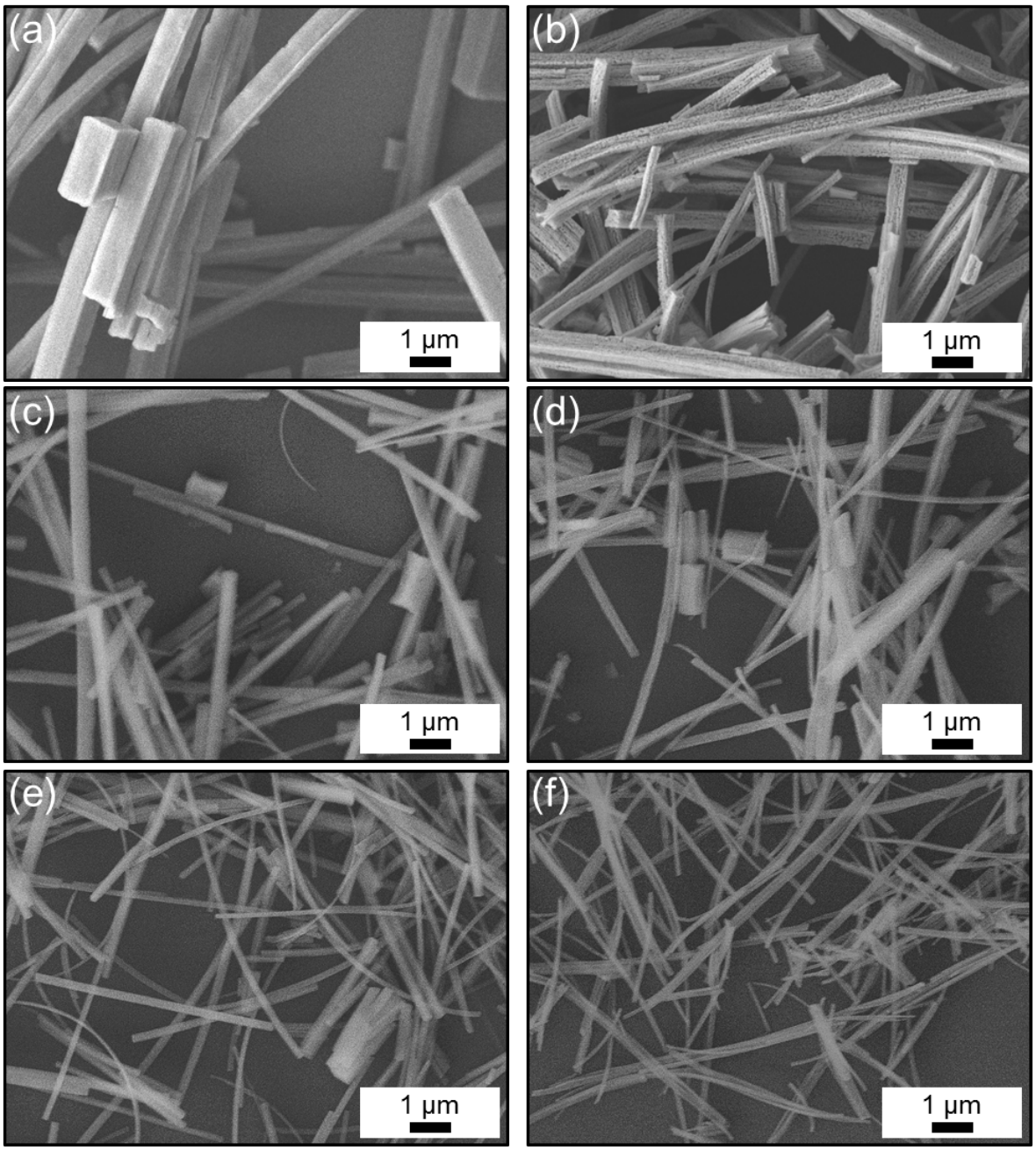

Fig. S1 Typical SEM images of $ZnFe_2(C_2O_4)_3$ NWs (a, c, and e) prepared from different combinations of Zn:Fe precursors: nitrate-chloride (a), nitrate-nitrate (c), nitrate-acetate (e). SEM images of its corresponding ZFO NWs (b, d, and f) after the calcination route.

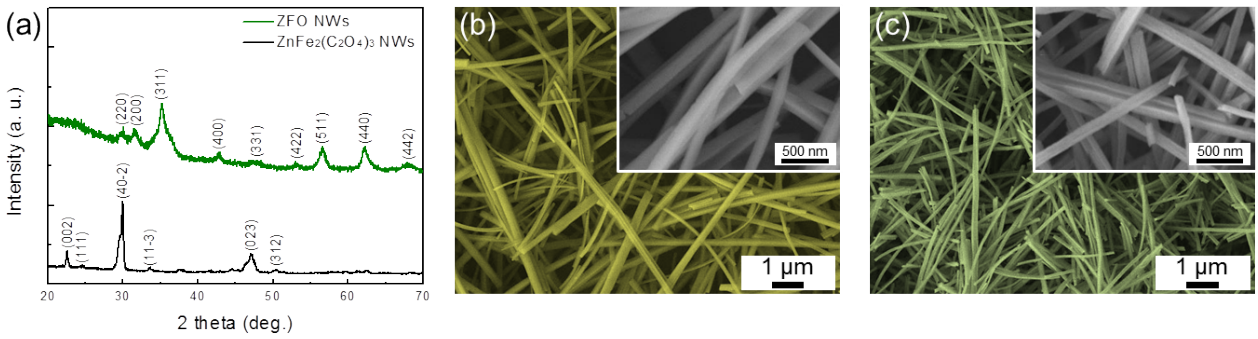

Fig. S2 (a) XRD patterns of the $ZnFe_2(C_2O_4)_3$ NWs and ZFO NWs. Typical SEM image of (b) $ZnFe_2(C_2O_4)_3$ NWs and (c) ZFO NWs.

The average crystallite size can be calculated from the full width at half maximum (FWHM) of the XRD peak of (311) plane using the Scherrer formula. The calculated crystallite size of the primary $ZnFe_2O_4$ particles was approximately 6.1 nm, which is in line with the values determined from TEM measurement shown in Fig. S4.

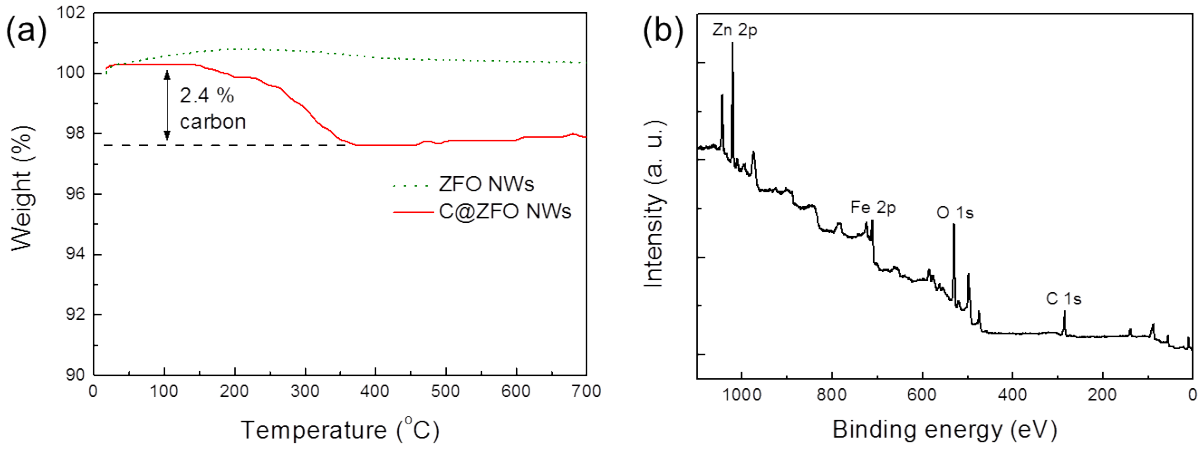

Fig. S3 (a) TGA curves of the non-carbon-coated ZFO NWs and C@ZFO NWs. The measurements were performed from room temperature to 700 °C at a heating rate of 10 °C min^{-1} in air. (b) XPS full spectra of the C@ZFO NWs.

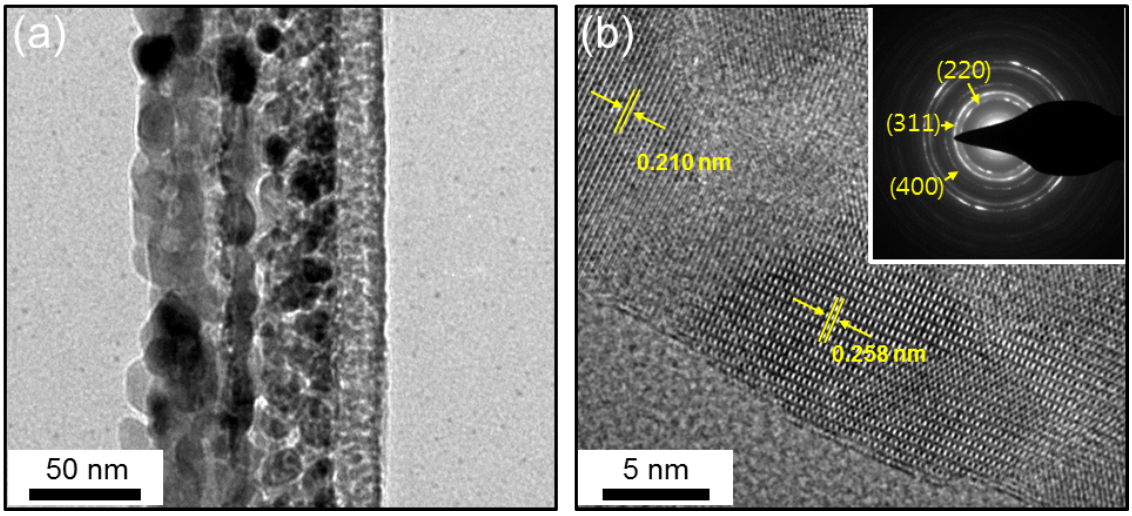

Fig. S4 (a) TEM and (b) HRTEM image of the non-carbon-coated ZFO NWs. The inset in panel (b) shows a corresponding SAED pattern.

As shown in Fig. S4a, the 1D ZFO NWs were also consisted of $ZnFe_2O_4$ nanoparticles with sizes of 5-20 nm. Interplane spacings of 0.210 and 0.258 nm were observed from HRTEM image (Fig. S4b), which is in accordance with the (400) and (311) planes of the spinel $ZnFe_2O_4$ phase, respectively. Note that the HRTEM image shows clean surface of ZFO NWs without the presence of outer carbon layers. Moreover, the polycrystalline nature of the ZFO NWs was also confirmed from the presence of multiple diffraction rings in the SAED patterns (inset of Fig. S4b).

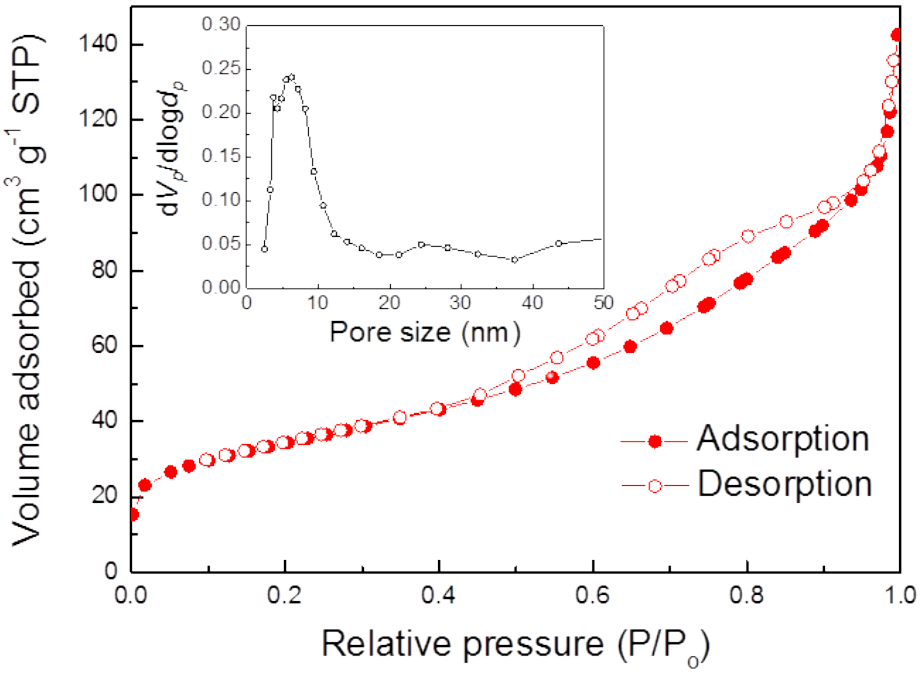

Fig. S5 Nitrogen adsorption/desorption isotherms of C@ZFO NWs. Inset shows corresponding pore size distribution of C@ZFO NWs.

The N_2 adsorption-desorption isotherms of the C@ZFO NWs were measured at 77 K. Fig. S5 shows the type IV N_2 adsorption-desorption isotherms of the C@ZFO NWs, which indicates a mesoporous material. From the adsorption branch of isotherm curves, the specific surface area of 120.1 m^2 g^{-1} is calculated through the BET method. Moreover, the average pore size of 7.5 nm is calculated using the BJH model.

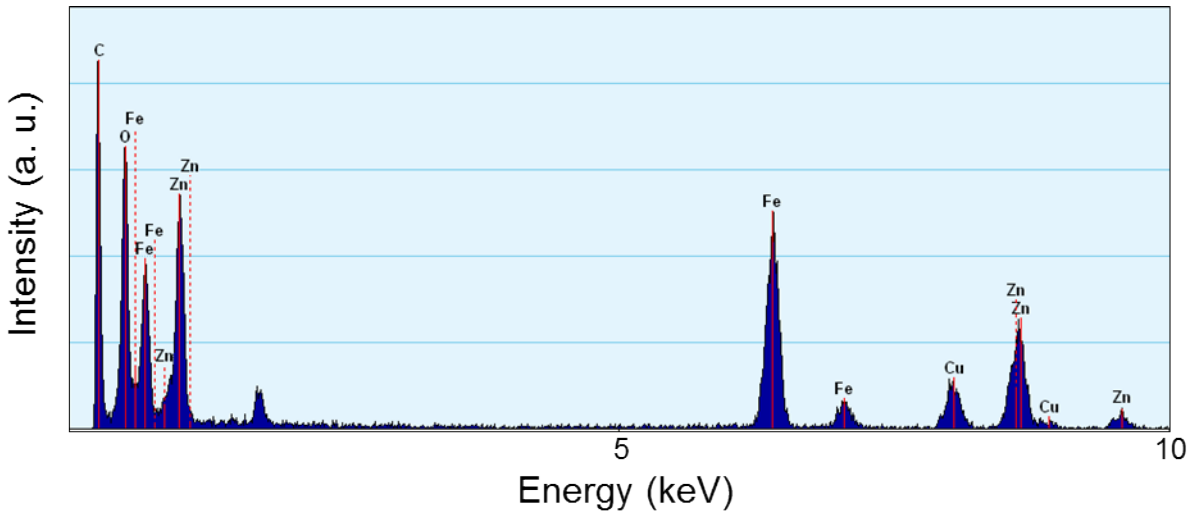

Fig. S6 EDX spectrum of the C@ZFO NWs.

Table S1 Summary of the cycle performance for as-prepared C@ZFO NWs, ZFO NWs, and ZFO NPs electrodes at a rate of 100 mA g^{-1}.

electrode	Initial C. E. [%][a]	1st cycle	100th cycle	Capacity retention after 1st cycle capacity [%]
		Discharge capacity [mAh g^{-1}]	Discharge capacity [mAh g^{-1}]	
C@ZFO NWs	82.1	1285.1	1292.1	100
ZFO NWs	76.1	1024.3	754.1	73.6
ZFO NPs	55.6	1148.7	96.9	8.4

[a]Initial coulombic efficiency (C. E.) is the ratio of the charge capacity to the discharge capacity during the first cycle.

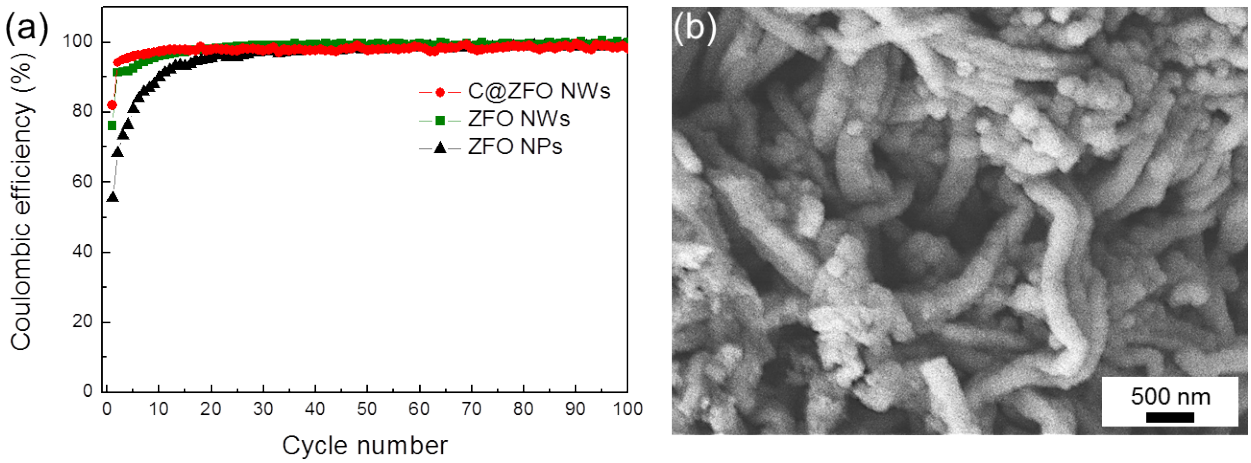

Fig. S7 (a) Coulombic efficiency-cycle number curves of the C@ZFO NWs together with ZFO NWs and ZFO NPs at a current rate of 100 mA g^{-1} in the potential window of 0.01–3.0 V. (b) Representative SEM images of the de-lithiated C@ZFO NWs electrode after 100 charge/discharge cycles.

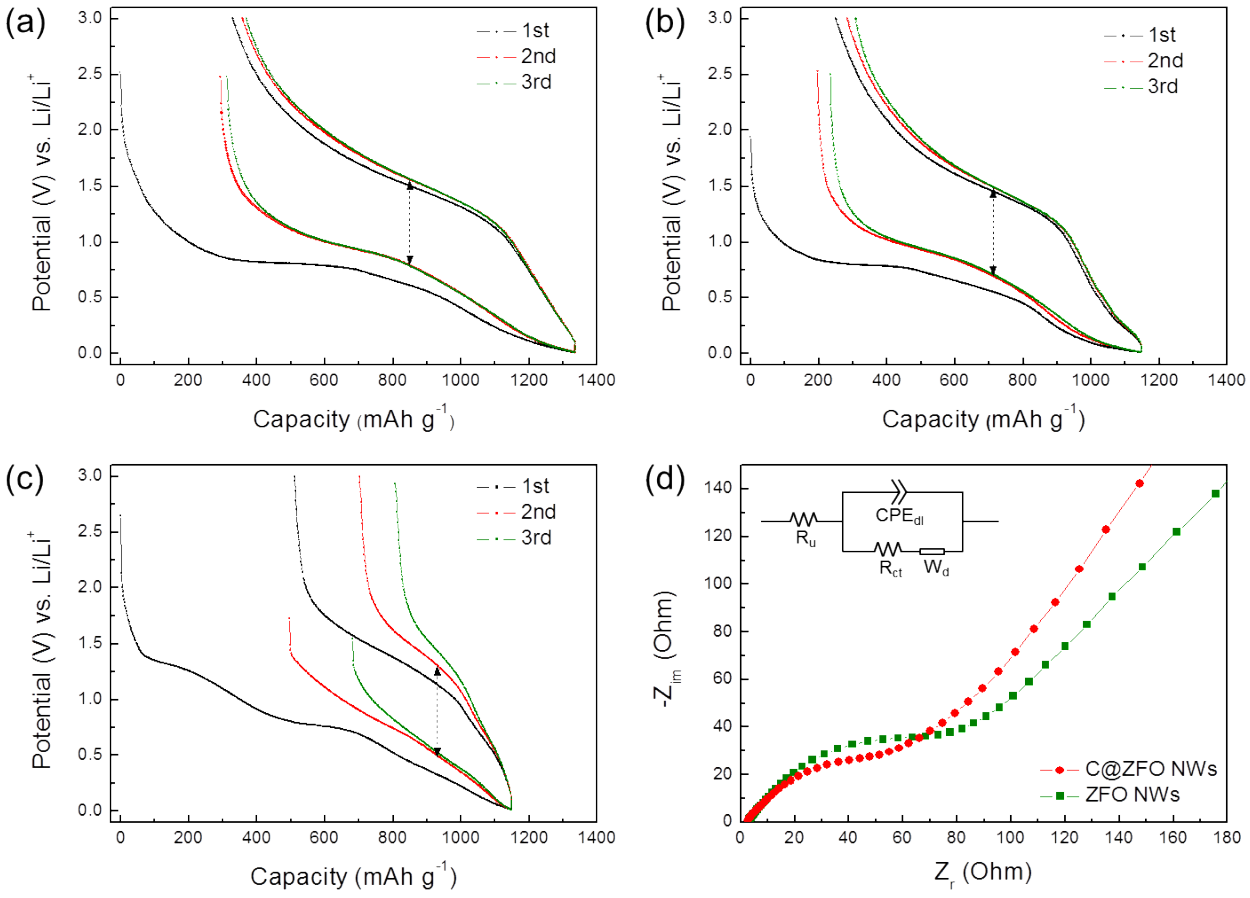

Fig. S8 Charge-discharge profiles of the (a) C@ZFO NWs, (b) ZFO NWs, and (c) ZFO NPs electrode at a rate of 100 mA g^{-1} in the potential window of 0.01–3.0 V. (d) Nyquist plots of the C@ZFO NWs and ZFO NWs measured at an open circuit voltage of 3.0 V after the first cycle. Inset shows the equivalent circuit. R_u is the uncompensated resistance, R_{ct} and CPE_{dl} are the charge transfer resistance and double layer capacitance, respectively. W_d is the Warburg impedance.

To further elucidate the enhanced kinetic properties of the C@ZFO NWs electrode as compared to the ZFO NWs electrode, electrochemical impedance spectroscopy measurements were conducted after the first cycle. As shown in Fig. S8d, the Nyquist plots consist of semicircles at high-to-medium frequency region and a sloping line at low frequency region. The Nyquist plots were fitted by equivalent circuits shown in inset of Fig. S8d. The high-frequency intercept of the semicircle is ascribed to the uncompensated resistance (R_u) which is due to particle-particle contact resistance, electrolyte resistance, and the resistance between electrode and current collector. The diameter of the medium-frequency semicircle corresponds to charge transfer resistance (R_{ct}) at the interface between electrode and electrolyte, and the low-frequency straight line is related to the Warburg impedance (W_d) due to Li^+ diffusion in the electrode material. From the Nyquist plots, R_{ct} of the C@ZFO NWs electrode is smaller than that of the ZFO NWs electrode system. A significant decrease of R_{ct} from 70.1 for the ZFO NWs to 48.5 Ω for the C@ZFO NWs indicates the improved electrical conductivity and Li^+ transfer rate by the carbon coating to the ZFO NWs because the faradic reaction is determined by both Li^+ ion transfer and electron conduction rate. Therefore, the C@ZFO NWs showed enhanced electrochemical properties compared to the non-carbon-coated ZFO NWs electrode system, as also demonstrated in the GITT measurements of Fig. 7.